Chapter 4

Light Emission from Graphene

Young Duck Kim and Myung-Ho Bae

Additional information is available at the end of the chapter

http://dx.doi.org/10.5772/64051

Abstract

Graphene has attracted great interest due to its superior and unique physical properties. The strong light-matter interaction with ultrafast and broadband photoresponse of graphene has allowed for the development of state-of-the art optical components, such as photodetectors and optical modulators, making this material very promising for ultrafast optical communications. However, so far, light emission from graphene has remained elusive, although this would open the door towards obtaining atomically thin, flexible and transparent light sources and graphene-based on-chip interconnects. In this chapter, we review experimental results and techniques of the electrically driven light emission from graphene in the infrared and visible spectrum range.

Keywords: Graphene, light emission, power dissipation, high electric field, Phonon temperature

1. Introduction

In order to obtain bright thermal radiation from gapless graphene, the radiative electron–hole recombination process is not enough due to the ultrafast energy relaxation that occurs through electron–electron (~10 fs) and electron–phonon (~1 ps) interactions. On the other hand, graphene's superior mechanical strength, high-temperature stability and non-equilibrium electron temperature, compared to lattice temperature, may enable the efficient thermal radiation under high electric field. However, the thermal radiation from electrically biased graphene is significantly influenced by the substrate. Especially, dominant vertical heat dissipation through underlying substrate, and extrinsic scattering effects, such as charged impurities and the surface polar optical phonon, limit the thermal radiation efficiency of graphene.

Freely suspended structure enables the dramatic suppression of undesirable vertical heat dissipation and extrinsic scattering effects by substrate, and much more promising to yield efficient and brighter thermal radiation from graphene in the infrared to visible range. Furthermore, the emitted light from suspended graphene interacts with the reflected light from the separated substrate surface, resulting in interference effects that can be used to tune the radiation spectrum of this material. Electro-thermal engineering will allow obtaining advanced graphene light emitters for atomically thin, flexible and transparent lighting and ultrafast optical interconnects. In this chapter, we will provide an overview of the thermal radiation from electrically biased graphenes in the infrared and visible spectrum range.

2. High electric field transport in graphene on substrate

Graphene's superior electronic [1], mechanical [2] and thermal [3] properties can be used for high mobility field-effect transistors (FETs) [4] and mechanical resonators [5]. In the case of electronic devices, as shown in **Figure 1a**, that depicts a graphene FET, the applied electric field applied by the source-drain voltage generates a Joule self-heating effect, which leads to a change of its electronic transport behaviour or device failure, in some cases [6]. For carbon nanotubes (CNTs), the observed electronic transport characteristics have been explained by heat transports along the CNT channels and between CNTs and the substrates [7]. There have been reports on the heat dissipation from graphene devise in a diffusive regime, where the chemical potential changes along the graphene channel. A direct method to study the heat dissipation is to accurately measure the temperature during device operation (see Sections 2.1–2.3). The temperature measurement of graphene on a substrate biased by a source–drain voltage has been performed in four ways: (1) shift of Raman peaks [8–11]; (2) thermal scanning imaging [11]; (3) thermal radiation [9, 10, 12] and (4) ratio of the Stoke/anti-Stoke intensities in Raman spectroscopy [9, 10, 13]. Methods (1) and (2) are sensitive to the acoustic phonon (AP) temperature (T_{ap}), while methods (3) and (4) are linked to the electron and optical phonon (OP) temperatures (T_e and T_{op}), respectively.

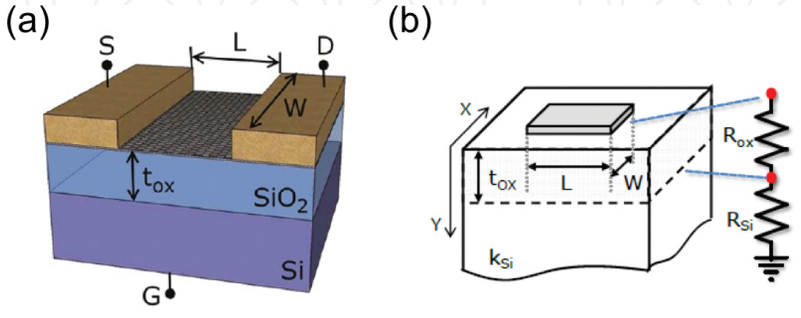

Figure 1. (a) Graphene field-effect transistor. S, D and G are source, drain and gate, respectively. *L* and *W* are length and width of graphene channel, respectively, and t_{ox} is thickness of SiO_2 layer [14]. (b) Thermal model for a graphene on SiO_2/Si substrate. R_{ox} and R_{Si} are thermal resistance of the oxide and silicon substrate, respectively. K_{si} is thermal conductivity of Si substrate.

http://dx.doi.org/10.5772/64051

The Fourier's law for thermal conductance is:

$$\dot{Q} = G_{th}\,\Delta T, \tag{1}$$

where $\dot{Q}$ is the amount of heat transferred per unit time, ΔT is the temperature difference between two points of interest, and G_{th} is the thermal conductance. Here, the temperature corresponds to T_{ap} since the acoustic phonons are the main contributors to heat conductions. **Figure 1b** shows how to apply the Fourier's law to graphene devices on a substrate, where R_{ox} and R_{Si} are the thermal resistances of the SiO_2 layer and Si substrate, respectively. The spreading thermal resistance of the Si substrate is given by $R_{Si} \sim 1/[2k_{si}(LW)^{1/2}]$ and $R_{ox} \sim t_{ox}/(k_{ox}LW)$, where $k_{ox} = 1.3\ Wm^{-1}K^{-1}$ and $k_{si} = 50\ Wm^{-1}k^{-1}$ are the thermal conductivities of the SiO_2 layer and Si substrate at room temperature, respectively [12]. t_{ox} is the thickness of SiO_2 layer, and L (W) is the length (width) of the graphene channel. Eq. (1) can also be expressed as $\Delta T = R_{th} P$, where R_{th} is the total thermal resistance, and P is the electrical power.

Figure 2 shows a summary of temperature increase (ΔT) of graphene devices on substrates, as a function of electrical power density, determined by various temperature measurement techniques. The closed, opened and half-closed scattered points show the acoustic, T_{ap}, T_{op} and T_e and electron temperatures, respectively.

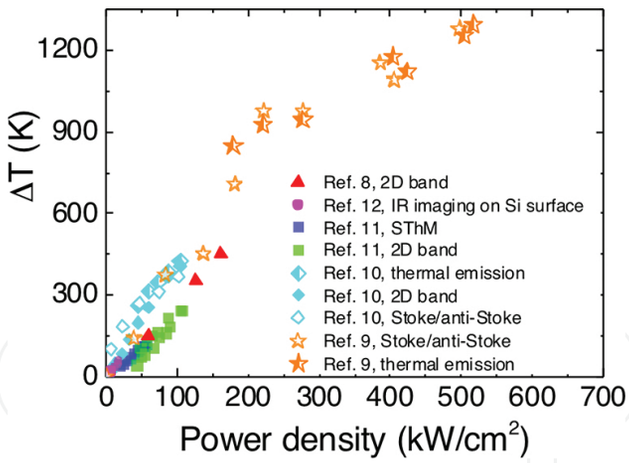

Figure 2. averaged temperature increase (ΔT) as a function of applied power per unit area of reported devices. Detailed information of each device is described in **Table 1**.

The detailed measurement techniques can be found in the legend of **Figure 2**. For each sample, one can obtain the R_{th} of the system, through the slope data plotted in **Figure 2**. **Table 1** and **Figure 3** show the R_{th} comparison between the experiments and calculations, based on the relation: $R_{th} \approx R_{ox} + R_{Si}$ (see **Figures 1b** and **3**).

References	L [μm]	W [μm]	t_{ox} [nm]	R_{ox} [K/W]	R_{Si} [K/W]	R_{cal} [K/W]	R_{exp} [K/W]
[8]	2.65	1.45	300	60,000	5100	65,100	73,500
[12]	28	6	300	1370	770	2140	2100
[11]	7	4	300	8240	1900	10,130	8300
[10]	4.15	1.45	300	38,350	4070	42,430	68,100
[9]	3.6	1.6	280	37,400	4160	41,560	69,800

Table 1. Summary of reported the thermal resistance of SiO_2 layer (R_{ox}), and Si substrate (R_{si}) with calculated (R_{cal}) and experimentally measured (R_{exp}) total thermal resistance, where all samples are placed on SiO_2/Si substrates.

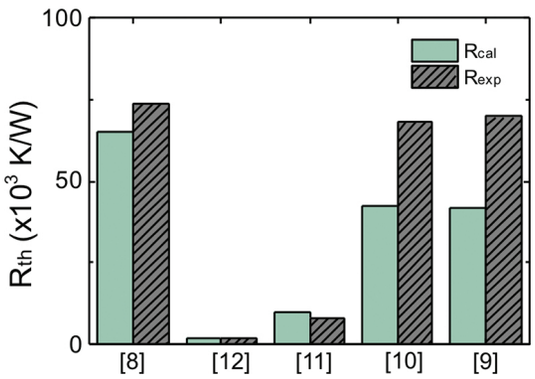

Figure 3. Average calculated (R_{cal}) and measured (R_{exp}) total thermal resistance of each reference, where R_{cal} and R_{exp} were adopted from **Table 1** for corresponding references.

In order to treat the heat transfer from graphene on a substrate into the surrounding environment, as shown in **Figure 1b**, let us first consider a one-dimensional heat equation along the graphene channel [12]:

$$\frac{d^2T}{dx^2} + p = \frac{g}{k_g A}(T - T_0), \tag{2}$$

where g is the thermal conductance of the substrate per unit length, k_g is the thermal conductivity of graphene, A is the cross-section of graphene, $p = I F_x$, I is the current and F_x is the electric field at x. For simplicity, if we consider an infinitely long graphene channel without bias current, Eq. (2) has a solution, $\Theta = \Theta(0)e^{-x/L_H}$, where $\Theta(x) = T(x) - T_0$ and $L_H = \sqrt{k_g A / g}$. The L_H is the lateral temperature diffusion (healing) length from a heat source through the graphene. The heat in a graphene device on a substrate is dissipated into a heat sink ($T = T_0$) mainly in two means: a direct way through the substrate underneath graphene or indirect way via metal contacts. In a graphene device where L is comparable to L_H, the heat dissipation through the metal contacts becomes important. In the opposite case of $L >> L_H$, the heat flow through the substrate is the dominant heat dissipation path. g is approximately given by $1/[L(R_{ox}+R_{Si})]$ (also see **Figure 1b**). For a monolayer graphene device on 300 nm thick, SiO_2/Si substrate with L =

http://dx.doi.org/10.5772/64051

25 μm, $W = 6$ μm and graphene thickness $t_g = 0.35$ nm, we get $L_H \approx \sqrt{\frac{t_{ox} t_g k_g}{k_{ox}}} \approx 0.2$ μm [12]. Here, we used the thermal conductivity of a few μm size graphene on a substrate as $k_g \sim 600$ $Wm^{-1}K^{-1}$ [15]. Thus, in general, graphene devices of few micrometres in length directly dissipate their heat through the substrate underneath graphene, and the temperature profile of the graphene reflects the heat generation profile.

2.1. Electron temperature of graphene

Thermal radiation can be observed for graphene devices on a substrate under high electric field, which is attributed to the electrically driven spontaneous emission from hot electrons of graphene [9, 10]. The thermalized charge carriers under electric field emit electromagnetic radiation, according to Planck's law, as a grey body:

$$I(E,T_e) = \varepsilon(E)\frac{2E^3}{h^2C^2}\left[\exp\left(\frac{E}{k_B T_e}\right) - 1\right]^{-1}, \tag{3}$$

where $I(E,T_e)$ is the spectral radiance, $\varepsilon(E)$ is the emissivity of graphene, E is the energy of the emitted photon, h is Planck's constant, c is the speed of light, and k_B is the Boltzmann constant.

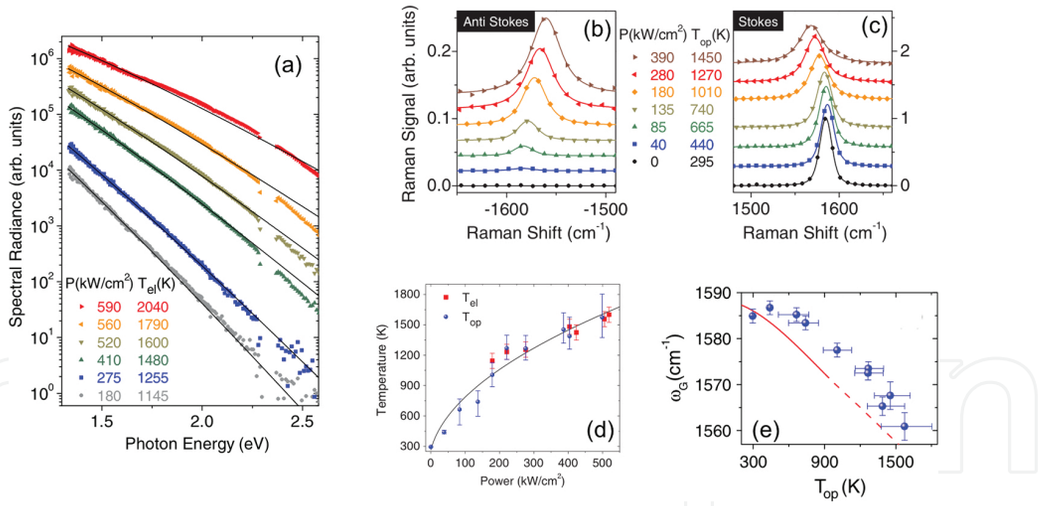

Figure 4. (a) Thermal radiation spectrum from graphene on substrate under applied electrical power per unit area (symbols). The radiation spectra are well fitted to Planck's law (solid line) and electron temperatures are estimated. (b) Anti-stoke and (c) Stokes Raman G mode as function of applied electric field and optical phonon temperature are indicated. (d) Electron and optical phonon temperature as function of the dissipated electrical power. It indicates the equilibrium of electron and optical phonon temperature. (e) Raman G mode frequency (symbol) features as function of optical phonon temperature. Solid line is the theoretically predicted temperature dependences under phonon equilibrium. Dashed line is linearly extrapolation (from Ref. [9]).

The T_e, extracted from its thermal radiation spectrum in the range of 1.3–2.6 eV, was of 1000–2000 K [9], as shown in **Figure 4a**. From the extracted T_e, we can assume that the strong electron-

electron interaction rapidly thermalizes electrons and holes, and attains hot charge carriers by the applied electric field. Furthermore, the experimentally measured emissivity $\varepsilon(E)$ of graphene of $=1.6 \pm 0.8$ % is consistent with the measured absorptivity $\alpha = 2.3$ % for monolayer graphene [9, 10]. This means that, for graphene under high electric field, Kirchhoff's law is valid in the measured energy range.

2.2. Optical phonon temperature of graphene

Raman spectroscopy is a well-known technique for the characterization of a number of layers, doping level, mechanical strain and temperature of graphene. In particular, for graphene devices under high electric field, Raman spectroscopy accurately provides the phonon temperature and population. In typical Raman spectroscopy, spontaneous Raman effects are due to the inelastic light scattering, with optical phonon modes of the material being determined by measurement. The resulting inelastic scattered of excited photon emits or absorbs optical phonons. The Stoke process involves the creation of extra optical phonons (n+1), and the anti-Stoke process is the annihilation of optical phonons (n).

In graphene, the phonon population for zone centre optical phonons can be estimated from the G peak signal intensity of the Raman spectra, which is proportional to phonon populations with effective temperature, and follows from the Bose-Einstein distribution. Raman signal intensity ratio of the anti-Stoke (I_{AS}) and Stokes (I_S) process is as follows:

$$\frac{I_{AS}}{I_S} \approx \exp(-\frac{\hbar\omega_G}{k_B T_{op}}), \tag{4}$$

where $\hbar\omega_G$ is the energy of G phonon. Experimentally, T_{op} is extracted from the ratio I_{AS}/I_S as shown in **Figure 4b** and **c**. Due to the high optical phonon energy of graphene, anti-Stoke Raman signals can be observed only above 440 K [9, 10, 13].

2.3. Acoustic phonon temperature of graphene

The Raman spectrum of graphene also exhibits a downshift of the Raman peak position with increasing temperature. This is due to the anharmonic coupling effect and anharmonic temperature of secondary phonons into G mode phonon decay and a thermal expansion effect [16]. Empirically, the down shift of the G peak can be measured as a linear function of T_{ap} as:

$$\omega_G = \omega_G^0 + \chi T_{ap}, \tag{5}$$

where ω_G^0 is the G peak frequency at zero temperature, and χ is the coefficient for temperature correction term of -0.016 $cm^{-1} K^{-1}$ [17], at moderate temperature.

2.4. Non-equilibrium phonon population in graphene

As discussed in Sections 2.1–2.3, accurate measurements of graphene temperature provide a deep understanding of the heat dissipation mechanism and electron-phonon interaction in biased graphene devices. Direct comparison of T_e and T_{op} temperatures of electrically biased graphene on a substrate shows that the T_e and T_{op} are in equilibrium up to 2000 K, as shown in **Figure 4d**.

In the case of CNTs, non-equilibrium phonon distributions have been measured when electrically biased, as high-energy optical phonons have larger populations than low-energy phonons, such as radial-breathing mode and acoustic phonons [7, 18].

Similarly to what was found with CNTs, non-equilibrium phonon populations in electrically biased graphene on a substrate have been observed. **Table 1** and **Figure 3** [9, 10] showed that the elevated T_{op} could be estimated by the ratio of Stoke/anti-Stoke intensity of G phonons and T_e measured by the thermal emission. For both cases, the experimentally obtained thermal resistance, R_{exp} is much larger than the predicted thermal resistance, R_{cal}, which could be due to the optical phonons and electrons not being in equilibrium with the acoustic phonon. This is consistent with the observation of the temperature deviation between T_{op} and the anharmonic temperature of secondary phonons, for which G phonons decay for $T_{op} > 670$ K [9]. From the device case in Ref. [10], the anharmonic temperature extracted from the 2D band showed similar temperatures to the T_{op} and T_e up to $T_{op} \sim 720$ K. In the reports, however, we should note that the temperature calibration for the 2D band was only obtained for $83\ \mathrm{K} < T < 373\ \mathrm{K}$, while the measurements was performed at $300\ \mathrm{K} < T < 700\ \mathrm{K}$, thus temperature correction could be needed for the high temperature region.

Experimental results show that strong electron-optical phonon coupling enables the equilibrium of the electron and optical phonon temperature, whereas an energy relaxation bottleneck to low-energy phonons results in the non-equilibrium phonon population. Furthermore, strong coupling with surface polar optical phonons and substrate acoustic phonons provides an extra electronic energy relaxation path, resulting in the effective cooling of acoustic phonons of graphene, under high electric field. Therefore, non-equilibrium optical phonon temperature (T_{op}) is given by:

$$T_{op} = T_{ap} + \alpha(T_{ap} - T_0), \tag{6}$$

where T_o is the ambient temperature environment, and α is the non-equilibrium coefficient. The α is defined by [7]:

$$\alpha = \frac{R_{op}}{R_{ap}}, \tag{7}$$

where R_{op} and R_{ap} are the thermal resistances related to optical phonon decay into acoustic phonons, and the heat conduction of acoustic phonons into the heat sink, respectively. Thus,

the T_{ap} and T_{op} are given by $T_{ap} = T_0 + PR_{ap}$ and $T_{op} = T_{ap} + PR_{op}$, respectively. For the devices from reference [9, 10], R_{exp} was ~70,000 K/W while R_{cal} was ~40,000 K/W (see **Table 1** and **Figure 3**). Since R_{cal} corresponds to R_{ap} and $R_{exp} \sim R_{ap} + R_{op}$, we get $R_{op} \sim 30{,}000$ K/W, resulting in $\alpha \sim 0.75$.

3. Infrared light emission from graphene on substrate

Graphene has unique electronics and phonon states under high electric field, such as decoupled electrons and low-energy phonon temperature [9, 13]. These make graphene an efficient material as thermal radiation source, determined only by T_e. Furthermore, gapless graphene exhibits high performance for optoelectronics such as photodetectors, optical modulator and plasmonic devices in the infrared range. Developing a high-speed and efficient infrared light source from graphene has a great potential for optical communications, as well as medical applications.

Previous studies of infrared light emission from graphene were accomplished by graphene FETs on a substrate under high electric field [9, 10, 12]. Due to the self-heating effect of graphene under electrical bias, only a small fraction ($<10^{-6}$) of energy is converted into light and most of the energy is dissipated into the substrate and metal contact. The extracted T_e of graphene light sources was reported to be in the range of 700–2000 K [9, 10].

In graphene FETs, charge carrier density profiles are determined by applied electric field and gate voltage. According to the self-consistent electrical-thermal model of charge and heat

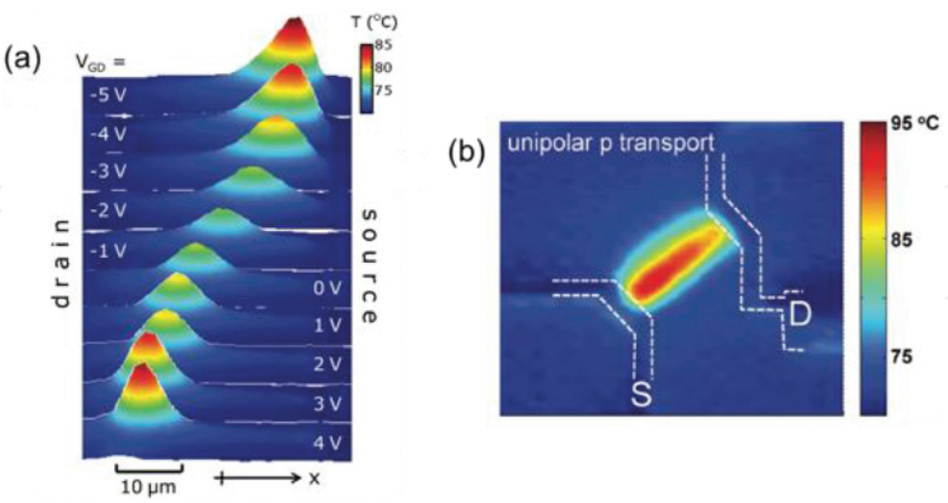

Figure 5. (a) Infrared mapping of temperature profiles along the graphene,showing hotspot formation. The hot spot moves from source to drain, marking the location of minimum charge density and maximum electric field, following the device electrostatics (from Ref. [14]). (b) Imaged temperature map of belayed graphene field-effect transistor (from Ref. [12])).

transport in graphene, the minimum charge carrier density spatial location is the cross-point of the Fermi level across the charge neutrality point. The hot spot position of the infrared image directly reveals the spatial location of the charge neutrality point along the graphene channel, as shown in **Figure 5a** and **b**. In some case, the stationary hot spot of infrared light emission, even under variation of gate voltages and source-drain bias, is attributed to the defects of graphene and trapped charges in the substrate [10, 12, 14].

Spontaneous thermal radiation is governed by the Fermi's golden rule, and the transition rate is determined by the optical density of the environment. This was shown in Ref. [19], through an optical micro cavity controlled graphene infrared light source, with emission around 925 nm,. Due to the strong light-matter interaction of atomically thin graphene and the optical confinement effect, micro-cavity structures enable the control of 20-fold enhancement of photocurrent generation, which is spectrally selective near infrared thermal radiation. The thermal radiation confinement effect inhibits spontaneous thermal radiation wavelengths larger than the resonant wavelength of the optical cavity. The optical cavity-induced suppression of the radiative thermal radiation also leads to the self-heating effect in graphene, which is affected by non-radiative heat transfer through the substrate, metal electrodes and radiative heat transfer.

4. High electric field transport in suspended graphene

As discussed in the previous section, high electric field transport of graphene on a substrate is affected by the substrate and environmental conditions. Limited thermal radiation efficiency and electron temperature are due to the dominant heat dissipation to the substrate and extrinsic scattering effects, such as electron-hole puddle, trapped charges [20] and surface polar phonon [21]. According to some authors [22, 23], suspended graphene shows ultrahigh mobility and fractional quantum Hall effect at low temperature, with low electric field. Therefore, in order to observe the intrinsic properties of graphene under high electric field, suspended structures are essential.

In suspended graphene, the self-heating effect plays a role due to significantly reduced heat dissipation through the substrate. Thermally induced charge carriers, saturation velocity, charge carrier mobility and thermal conductivity of graphene are significantly affected by the applied electric field and temperature.

In the clean limit of suspended graphene, under high electric field as shown in **Figure 6a–c**, the total charge carrier density of graphene is dominated by thermally induced charge carriers (n_{th}), represented as:

$$n_{th} = \left(\frac{\pi}{6}\right)\left(\frac{k_B T}{\hbar v_F}\right)^2, \tag{8}$$

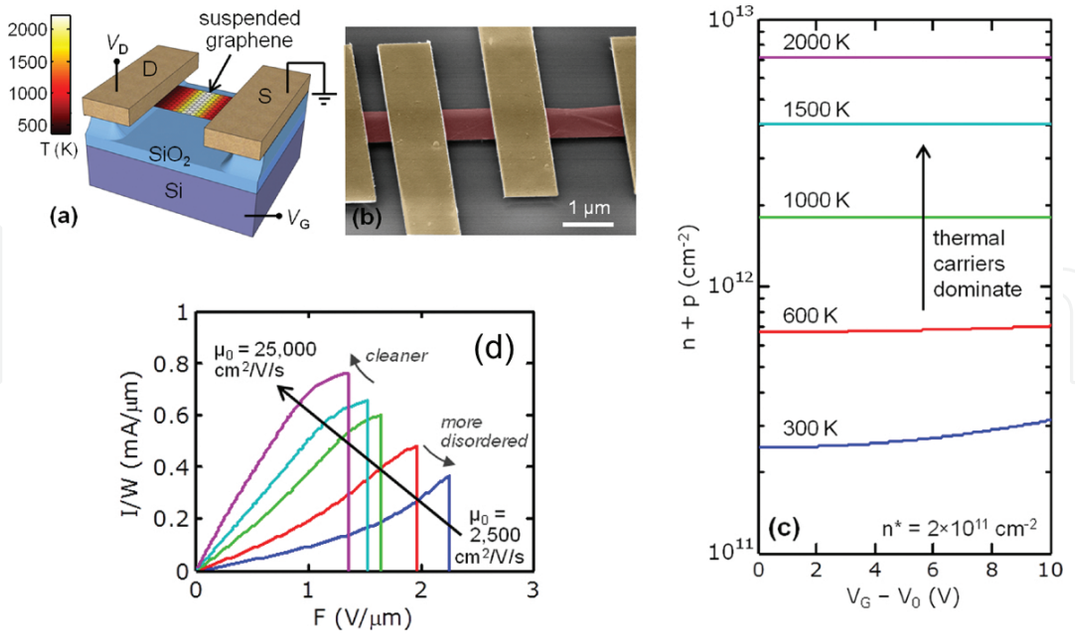

Figure 6. (a) Suspended graphene device, where colour scale indicates the temperature under high electric field. (b) SEM image of suspended graphene grown by CVD. (c) Calculated total charge carrier density as function of gate voltage with increasing temperature. In suspended graphene, thermally generated charge carriers are dominant at high temperature and independent of gate voltage. (d) Simulated *I*/*W* versus *F* with variation of low-field mobility-based electro-thermal self-consistent simulation (from Ref. [24]).

where v_F is the Fermi velocity of graphene. The intrinsic carrier density of graphene is $n_i = 4(n_{th}^2 + (n_{pd}/2)^2)$, where n_{pd} is electron-hole puddle-induced carriers. The carrier density induced by electrostatic gate V_g is $n_g = C_{ox}(V_{dr} - V_g)/e$, where V_{dr} is the charge neutral voltage of graphene. In total, the electron (hole) carrier density (see **Figure 6c**) is as follows:

$$n_e(n_h) = \frac{1}{2}\left(\pm n_g + \sqrt{n_g^2 + n_i}\right). \tag{9}$$

The current density J in the suspended graphene, with an applied electric field, is presented by the continuity equation:

$$J = e(n_{ex} + n_{hx})v_{dx}, \tag{10}$$

where e is the electron charge, n_{ex} (n_{hx}) is the electron (hole) density, v_d is the drift velocity along the graphene channel. The drift velocity is expressed by:

$$v_{dx} = \frac{\mu_x F_x}{[1 + (\mu_x F_x / v_{sat})^{\eta}]^{1/\eta}}, \tag{11}$$

where μ_x is the temperature dependent charge carrier mobility, F_x is the electric field along the graphene channel, and v_{sat} is a the saturation velocity determined by the intrinsic graphene optical phonon (160 meV) scattering [24, 25].

For a self-consistent electrical-thermal calculation of suspended graphene, the heat diffusion equation for the temperature profile (T_x) along the graphene channel takes the from:

$$\frac{d^2T_x}{dx^2} + \frac{1}{k_x Wt}\frac{dP_x}{dx} - \frac{2g_x}{k_x t}\left(T_x - T_0\right) = 0, \tag{12}$$

where P_x (= $I(V_x - IR_c)$) is the local dissipated electrical power, k_x is the temperature dependent thermal conductivity, W is width, t is thickness, g_x is the thermal conductance per unit area ($g_x \sim 0$ in vacuum), and T_0 is ambient temperature. Assuming that the temperature-dependent charge carrier mobility is considered, $(T_e) = \mu_0 (T_0 / T_e)^{\beta}$, where μ_0 is the ambient temperature mobility, T_e is the electron temperature, and β varies from 1.5 to 2.5, depending on the kind of sample. Furthermore, thermal conductivity is assumed to be $k(T_{ap}) = k_0 (T_0 / T_{ap})^{\gamma}$, where k_0 is the ambient temperature thermal conductivity, T_{ap} is the acoustic phonon temperature of graphene, and γ varies from 1.7 to 1.9 depending on the kind of sample.

Using a self-consistent electrical-thermal calculation in suspended graphene, as shown in **Figure 6d**, clean samples show the saturation behaviour under high electric field. This implies that high charge carrier mobility of suspended graphene devices have a larger temperature dependence ($\beta \sim 2.5$) due to the strong electron-intrinsic graphene optical phonon interactions. However, disordered suspended graphene shows superliner behaviour and less dependence on temperature ($\beta \sim$ 1.5). This is due to dominant hopping transport with increase of thermally generated charge carriers under high electric field [24].

In contrast with suspended CNTs, suspended graphene does not show a negative differential conductance, due to the linear increase of density of states in 2D, whereas CNTs have strong 1D phonon scattering, resulting in a negative differential conductance [7].

Along the temperature profile of suspended graphene, drift velocity and charge carrier density are affected by current density. Theoretically, saturation velocity of graphene was predicted as $v_{sat} \sim 2.7 \times 10^7 cm/s$, which is limited by 160 meV intrinsic graphene optical phonons [26]. Experimentally, saturation velocity before breakdown is measured as $v_{sat} \sim 1.7 \times 10^7 cm/s$ [24]. Of course, in a suspended graphene structure, flexural phonons [27] cannot be ignored, as they may be one of reasons for variation in saturation velocity.

Suspended graphene is well known as a material having the highest thermal conductivity at room temperature ($k_0 \sim$ 2500 W/mK). However, thermal conductivity of suspended graphene displays an abrupt decrease ($\sim T^{-1.7}$) at high temperature [24]. This is attributed to the flexural phonons modes which enable strong second-order three-phonon scattering [28] ($\sim T^{-2}$) and first-order Umklapp phonon–phonon scattering ($\sim T$). The estimated average

thermal conductivity of electrically biased suspended graphene at 1000 K is of $\sim 310\ W/mK$, for both mechanically exfoliated and chemical vapour deposited (CVD) grown graphene.

5. Bright visible light emission from suspended graphene

Graphene has a great potential as an efficient thermal radiation light source due to its superior mechanical strength, high-temperature stability, high current density and non-equilibrium phonon modes. However, previous reports regarding the thermal radiation of supported graphene [9, 10, 12, 19] have been limited to the near infrared light emission range, and extremely small fractions of electrical power are converted into the photons ($\sim 10^{-6}$). The main reason for the limited performance of graphene light emitters supported on a substrate is the dominant heat dissipation through the substrate, and significant hot carriers cooling by dominant extrinsic scattering origins, such as charged impurities, trapped charges and surface polar phonons. In the case of freely suspended graphene, these issues can be ignored. Therefore, suspended structures are promising for the observation of bright, efficient light emission radiation approaching the intrinsic properties.

There are several methods that can be used for the synthesis of suspended graphene structures. One is wet-etching of a sacrificial layer after metallization onto the graphene. The other procedure is the transfer of patterned graphene onto pre-fabricated trench substrate. In order to increase the fabrication yield and prevent the collapse of graphene, a critical point dryer process is important. Suspended graphene structures are fabricated using mechanically

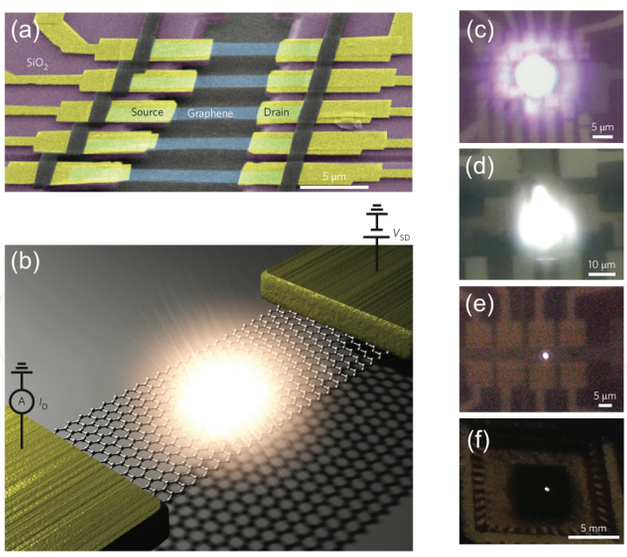

Figure 7. (a) SEM image of suspended monolayer graphene devices. (b) Schematic of electrically biased suspended graphene and light emission from the centre of graphene. Micrographs of bright visible light emission from a suspended mechanically exfoliated graphene: (c) few-layer graphene under $V_{sd} = 2.90$ V, (d) multi-layer graphene under $V_{sd} = 7.90$ V, and (e) monolayer graphene $V_{sd} = 2.58$ V. (f) Optical image of remarkably bright visible light emission from a suspended few-layer graphene, which is visible even to the naked eye (from Ref. [25])

exfoliated graphene or large-scale graphene grown by the CVD method. **Figure 7a** shows the obtained suspended graphene devices [25].

In order to observe light emission from suspended graphene under electrically bias, an experimental set-up, similar to that shown in **Figure 7b**, is used under vacuum ($\sim 10^{-5}$ Torr), at room temperature. In addition, to get clean graphene channel and reliable contact resistance, a slow current-induced annealing process [29] is essential. Suspended graphene exhibits bright visible light at the centre of the graphene channel once the applied bias voltage exceeds the critical field ($0.5 \sim 1.0$ V/μm), as shown in **Figure 7c–e**. The intensity of visible light is remarkably intense and can even be observed by the naked eye, without additional magnification, as shown in **Figure 7f**.

Y.D. Kim et al. [25] also demonstrated multiple visible light emission from a large-scale suspended graphene array, which was fabricated from large-scale CVD graphene. The synthesis of a large-scale, robust and bright visible light emitter array from CVD graphene will allow obtaining graphene-based flexible and transparent lighting and display modules. Furthermore, complementary metal-oxide-semiconductor (CMOS) compatibility of graphene technology will enable a hybrid graphene-photonic platform for ultrafast optical communications.

The radiation spectrum from electrically biased suspended graphene over a trench of depth ($D \sim 1000$ nm) exhibits multiple emission peaks in the visible range, as shown in **Figure 8a**. These multiple emission peaks are quite interesting, since graphene is a gapless material, and the radiation spectrum was predicted to follow the featureless Planck's law of a grey body (Eq. (3)). The multiple peaks in the visible range are strongly affected by the trench depth rather than by the number of layers of graphene and electronic band structure.

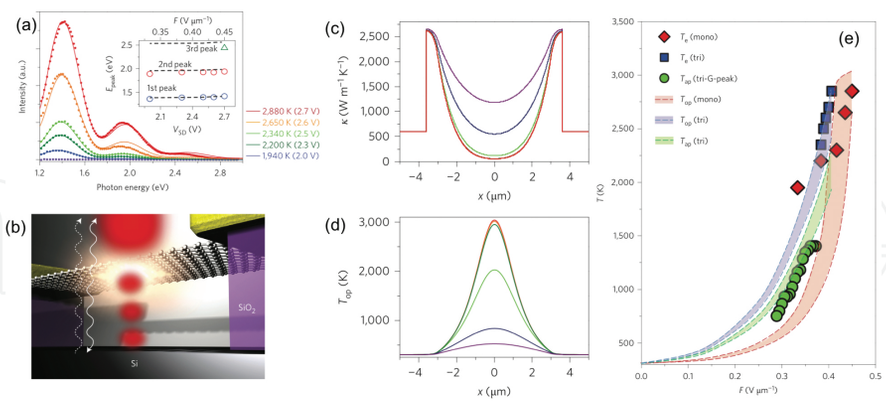

Figure 8. (a) Spectra of visible light emitted from electrically biased suspended graphene exhibiting multiple strong emission peaks. Thermal radiation with interference effect (solid line) fit well to the experimental data (symbol). Estimated electron temperatures of suspended graphene are indicated as function of applied source-drain bias. Inset: emission peak energies as a function of source-drain bias and applied electric field. (b) Interference effect between reflected (dashed arrow) and thermal radiation originated directly from graphene suspended over a trench. (c) Estimated thermal conductivity and (d) optical phonon temperature of suspended graphene based on self-consistent electrical and thermal transport, where it is assumed that $T_{op} = T_e$. (e) Measured temperature of graphene (symbol) and calculated temperature (dashed line) as function of applied electric field (from Ref. [25]).

These multiple emission peaks in the visible range and significant modulation by trench depth can be understood by interference effects between the light emitted directly from the suspended graphene and light reflected from the substrate as shown in **Figure 8b**. When we neglect the light reflection and absorption by the graphene, the interference effect on thermal radiation is given by:

$$I(\omega, D) = I_0(\omega)\left(\frac{1+|r(\omega)|}{2} + Re\left[r(\omega)\exp\left(\frac{i2\omega D}{c}\right)\right]\right), \quad (13)$$

where $I_0(\omega) \sim \omega^3 / (\exp(\hbar\omega / k_B T_e) - 1))$ is the thermal radiation intensity of suspended graphene, $r(\omega)$ is the reflection coefficient of Si substrate, ω is the photon frequency, is the emissivity of graphene, D is the trench depth, k_B is the Boltzmann constant, T_e is the electron temperature of graphene, and c is the speed of light [25]. A strong interference effect enables the selectively enhancement of thermal radiation from graphene at a certain wavelength and can increase the radiation efficiency through the engineering of interference effects.

Based on thermal radiation with interference effect (Eq. 13), electron temperature of suspended graphene was extracted, as shown in **Figure 8a** (solid line) and approaches 2800 K. The light emission peak in the visible range rapidly increases with the applied electric field above a critical field ($\sim 0.4\ V/\mu m$). This is attributed to the accumulation of hot electrons and optical phonons in suspended graphene, above the critical field, which is related to the activation of intrinsic graphene optical phonons under an electric field. In suspended graphene, low activation to generate intrinsic optical phonons in an electric field are achieved by the reduction of energy loss suffered by electric field-induced hot electrons with extrinsic scattering sources, and prevent the direct cooling of hot electron and phonons through heat transfer to substrate. Current saturation in suspended graphene is observed and is known to be a signature of strong electron scattering by intrinsic optical phonons of graphene itself.

Raman spectroscopy provides an accurate measurement of acoustic phonons, optical phonon population and the temperature under applied electric field, as described in Sections 2.2 and 2.3. However, bright thermal radiation from electrically biased suspended graphene becomes significantly stronger than the Raman signal above ~1500 K. In order to estimate the temperature profiles and thermal conductivity, self-consistent numerical simulation of electrical and thermal transport is used, as described in Section 4. From numerical simulation based on the electrical transport data, thermal conductivity at the centre of the suspended graphene channel decreases from $k \sim 2700\ W/mK$ ($T_{ap} \sim 300$ K) to $k \sim 65\ W/mK$ ($T_{ap} \sim 1800$ K), as shown in **Figure 8c**. An abrupt decrease of thermal conductivity of suspended graphene also suppresses lateral heat dissipation along the graphene channel, meaning that hot electrons are confined and spatially localized at the centre of the graphene. As shown in **Figure 8d**, the maximum temperature is located at the centre of the graphene channel, which is consistent with the brightest light emission position as shown in **Figure 7**.

Effectively localization of hot electron in suspended graphene by unique electronic and thermal properties enables bright visible light emission. Based on the Stefan–Boltzmann law from measured electron temperature, as shown in **Figure 8e**, thermal radiation efficiency was estimated as ~ 4.45 $\times 10^{-3}$, which is a 1000-fold enhancement compared to the graphene devices on substrates ($\sim 10^{-6}$). Furthermore, engineering of radiation spectrum enhancement in the visible range provides the further enhancement of radiation efficiency.

An electrically driven graphene light emitter has great advantages, such as being atomically thin, broadband emission, radiation spectrum tunability, surface and self-emission all with a simple structure. Furthermore, ultrafast and broadband electrical and optical response of graphene has enabled the development of a nanoscale ultrafast light emitter. We expect to obtain atomically thin, flexible and transparent light sources and on-chip optical interconnects for communications based on graphene.

Acknowledgements

The authors thank J. Hone, Y.D. Park and G. Arefe. YDK was supported by Grants from ONR (N00014-13-1-0662 and N00014-13-1-0464) and DE-SC0012592. MB was supported by Grants from the National Research Foundation of Korea (NRF-2012-M3C1A1-048861, NRF-2015R1A2A1A10056103) funded by the Korean government.

Author details

Young Duck Kim[1*] and Myung-Ho Bae[2*]

*Address all correspondence to: yk2629@columbia.edu and mhbae@kriss.re.kr

1 Department of Mechanical Engineering, Columbia University, New York, NY, USA

2 Korea Research Institute of Standards and Science, Daejeon, Republic of Korea

References

[1] A K Geim and K S Novoselov. The rise of graphene. Nat Mater. 2007;6(3):183–191. doi: 10.1038/nmat1849

[2] Changgu Lee, Xiaoding Wei, Jeffrey W Kysar, and James Hone. Measurement of the elastic properties and intrinsic strength of monolayer graphene. Science. 2008;321(5887):385–388. doi:10.1126/science.1157996

[3] Alexander A Balandin, Suchismita Ghosh, Wenzhong Bao, Irene Calizo, Desalegne Teweldebrhan, Feng Miao, and Chun Ning Lau. Superior thermal conductivity of single-layer graphene. Nano Lett. 2008;8(3):902–907. doi:10.1021/nl0731872

[4] Y M Lin, C Dimitrakopoulos, K A Jenkins, D B Farmer, H Y Chiu, A Grill, and Ph Avouris. 100-GHz transistors from wafer-scale epitaxial graphene. Science. 2010;327(5966):662–662. doi:10.1126/science.1184289

[5] Changyao Chen, Sunwoo Lee, Vikram V Deshpande, Gwan-Hyoung Lee, Michael Lekas, Kenneth Shepard, and James Hone. Graphene mechanical oscillators with tunable frequency. Nat Nanotechnol. 2013;8(12):923–927. doi:10.1038/NNANO.2013.232

[6] Eric Pop. Energy dissipation and transport in nanoscale devices. Nano Res. 2010;3(3):147–169. doi:10.1007/s12274-010-1019-z

[7] Eric Pop, David Mann, Jien Cao, Qian Wang, Kenneth Goodson, and Hongjie Dai. Negative differential conductance and hot phonons in suspended nanotube molecular wires. Phys Rev Lett. 2005;95(15):155505. doi:10.1103/PhysRevLett.95.155505

[8] Marcus Freitag, Mathias Steiner, Yves Martin, Vasili Perebeinos, Zhihong Chen, James C Tsang, and Phaedon Avouris. Energy dissipation in graphene field-effect transistors. Nano Lett. 2009;9(5):1883–1888. doi:10.1021/nl803883h

[9] Stéphane Berciaud, Melinda Y Han, Kin Fai Mak, Louis E Brus, Philip Kim, and Tony F Heinz. Electron and optical phonon temperatures in electrically biased graphene. Phys Rev Lett. 2010;104(22):227401. doi:10.1103/PhysRevLett.104.227401

[10] Marcus Freitag, Hsin-Ying Chiu, Mathias Steiner, Vasili Perebeinos, and Phaedon Avouris. Thermal infrared emission from biased graphene. Nat Nanotechnol. 2010;5(7):497–501. doi:10.1038/nnano.2010.90

[11] Insun Jo, I-Kai Hsu, Yong J Lee, Mir Mohammad Sadeghi, Seyoung Kim, Stephen Cronin, Emanuel Tutuc, Sanjay K Banerjee, Zhen Yao, and Li Shi. Low-frequency acoustic phonon temperature distribution in electrically biased graphene. Nano Lett. 2011;11(1):85–90. doi:10.1021/nl102858c

[12] Myung-Ho Bae, Zhun-Yong Ong, David Estrada, and Eric Pop. Imaging, simulation, and electrostatic control of power dissipation in graphene devices. Nano Lett. 2010;10(12):4787–4793. doi:10.1021/nl1011596

[13] Dong-Hun Chae, Benjamin Krauss, Klaus von Klitzing, and Jurgen H Smet. Hot phonons in an electrically biased graphene constriction. Nano Lett. 2010;10(2):466–471. doi:10.1021/nl903167f

[14] Myung-Ho Bae, Sharnali Islam, Vincent E Dorgan, and Eric Pop. Scaling of high-field transport and localized heating in graphene transistors. ACS Nano. 2011;5(10):7936–7944. doi:10.1021/nn202239y

[15] Jae Hun Seol, Insun Jo, Arden L Moore, Lucas Lindsay, Zachary H Aitken, Michael T Pettes, Xuesong Li, Zhen Yao, Rui Huang, David Broido, Natalio Mingo, Rodney S Ruoff, and Li Shi. Two-dimensional phonon transport in supported graphene. Science. 2010;328(5975):213–216. doi:10.1126/science.1184014

[16] Nicola Bonini, Michele Lazzeri, Nicola Marzari, and Francesco Mauri. Phonon anharmonicities in graphite and graphene. Phys Rev Lett. 2007;99(17):176802. doi:10.1103/PhysRevLett.99.176802

[17] I Calizo, F Miao, W Bao, C N Lau, and A A Balandin. Variable temperature Raman microscopy as a nanometrology tool for graphene layers and graphene-based devices. Appl Phys Lett. 2007;91(7):07913. doi:10.1063/1.2771379

[18] Mathias Steiner, Marcus Freitag, Vasili Perebeinos, James C Tsang, Joshua P Small, Megumi Kinoshita, Dongning Yuan, Jie Liu, and Phaedon Avouris. Phonon populations and electrical power dissipation in carbon nanotube transistors. Nat Nanotechnol. 2009;4(5):320–324. doi:10.1038/nnano.2009.22

[19] Michael Engel, Mathias Steiner, Antonio Lombardo, Andrea C Ferrari, Hilbert v Löhneysen, Phaedon Avouris, and Ralph Krupke. Light–matter interaction in a microcavity-controlled graphene transistor. Nat Commun. 2012;3:906. doi:10.1038/ncomms1911

[20] Young Duck Kim, Myung-Ho Bae, Jung-Tak Seo, Yong Seung Kim, Hakseong Kim, Jae Hong Lee, Joung Real Ahn, Sang Wook Lee, Seung-Hyun Chun, and Yun Daniel Park. Focused-laser-enabled p–n junctions in graphene field-effect transistors. ACS Nano. 2013;7(7):5850–5857. doi:10.1021/nn402354j

[21] Inanc Meric, Melinda Y Han, Andrea F Young, Barbaros Ozyilmaz, Philip Kim, and Kenneth L Shepard. Current saturation in zero-bandgap, top-gated graphene field-effect transistors. Nat Nanotechnol. 2008;3(11):654–659. doi:10.1038/nnano.2008.268

[22] K I Bolotin, K J Sikes, Z Jiang, M Klima, G Fudenberg, J Hone, P Kim, and H L Stormer. Ultrahigh electron mobility in suspended graphene. Solid State Commun. 2008;146(9–10):351–355. doi:10.1016/j.ssc.2008.02.024

[23] Kirill I Bolotin, Fereshte Ghahari, Michael D Shulman, Horst L Stormer, and Philip Kim. Observation of the fractional quantum Hall effect in graphene. Nature. 2009;462(7270):196–199. doi:10.1038/nature08582

[24] Vincent E Dorgan, Ashkan Behnam, Hiram J Conley, Kirill I Bolotin, and Eric Pop. High-field electrical and thermal transport in suspended graphene. Nano Lett. 2013;13(10):4581–4586. doi:10.1021/nl400197w

[25] Young Duck Kim, Hakseong Kim, Yujin Cho, Ji Hoon Ryoo, Cheol-Hwan Park, Pilkwang Kim, Yong Seung Kim, Sunwoo Lee, Yilei Li, Seung-Nam Park, Yong Shim Yoo, Duhee Yoon, Vincent E Dorgan, Eric Pop, Tony F Heinz, James Hone, Seung-Hyun Chun, Hyeonsik Cheong, Sang Wook Lee, Myung-Ho Bae, and Yun Daniel Park. Bright

visible light emission from graphene. Nat Nanotechnol. 2015;10(8):676–681. doi: 10.1038/NNANO.2015.118

[26] Tian Fang, Aniruddha Konar, Huili Xing, and Debdeep Jena. High-field transport in two-dimensional graphene. Phys Rev B. 2011;84(12):125450. doi:10.1103/PhysRevB.84.125450

[27] Eduardo V Castro, H Ochoa, M I Katsnelson, R V Gorbachev, D C Elias, K S Novoselov, A K Geim, and F Guinea. Limits on charge carrier mobility in suspended graphene due to flexural phonons. Phys Rev Lett. 2010;105(26):266601. doi:10.1103/PhysRevLett.105.266601

[28] Denis L Nika, Artur S Askerov, and Alexander A Balandin. Anomalous size dependence of the thermal conductivity of graphene ribbons. Nano Lett. 2012;12(6):3238–3244. doi:10.1021/nl301230g

[29] J Moser, A Barreiro, and A Bachtold. Current-induced cleaning of graphene. Appl Phys Lett. 2007;91(16):1653513. doi:10.1063/1.2789673